Role of high-order lattice anharmonicity in the phonon thermal transport of silver halide AgX (X=Cl, Br, I)

Niuchang Ouyang[1], Zezhu Zeng[1,2,*] Chen Wang[1], Qi Wang[3], and Yue Chen[1†]
[1] *Department of Mechanical Engineering, The University of Hong Kong, Pokfulam Road, Hong Kong SAR, China*
[2] *Institute of Science and Technology Austria, Am Campus 1, 3400 Klosterneuburg, Austria*
[3] *Thermal Science Research Center, Shandong Institute of Advanced Technology, Jinan, Shandong Province 250103, China*
(Dated: July 30, 2023)

The phonon transport mechanisms and ultralow lattice thermal conductivities (κ_L) in silver halide AgX (X=Cl, Br, I) compounds are yet to be better understood. Herein, we study the lattice dynamics and thermal property of AgX under the framework of perturbation theory and the two-channel Wigner thermal transport model based on accurate machine learning potentials. We find that an accurate extraction of the third-order atomic force constants from largely displaced configurations is significant for the calculation of the κ_L of AgX, and the coherence thermal transport is also non-negligible. While in AgI, the calculated κ_L still considerably overestimates the experimental values even including four-phonon scatterings. Molecular dynamics (MD) simulations using machine learning potential suggest an important role of the higher-than-fourth-order lattice anharmonicity in the low-frequency phonon linewidths of AgI at room temperature, which can be related to the simultaneous restrictions of the three- and four-phonon phase spaces. The κ_L of AgI calculated using MD phonon lifetimes including full-order lattice anharmonicity shows a better agreement with experiments.

I. INTRODUCTION

Recently, silver halide AgX (X=Cl, Br, I) compounds exhibit promising photoelectrochemical and photocatalytic properties, which make them attractive for use in photovoltaic devices [1, 2]. Efficient thermal transport is crucial in such devices to prevent the buildup of heat and ensure optimal performance. Additionally, the thermal transport properties of AgX are also relevant in their potential use as solid-state electrolytes [3], which are crucial components in advanced energy storage and conversion systems, such as solid-state batteries and fuel cells. Understanding the heat transfer characteristics of AgX can help optimize their use as electrolytes and minimize energy losses due to thermal inefficiencies. Moreover, AgX have also been demonstrated as high-performance thermoelectric materials due to the ultralow intrinsic lattice thermal conductivities (κ_L) [4]. However, a better understanding of the phonon thermal transport mechanisms of AgX is still in its infancy. Therefore, studying the thermal transport properties of silver halide AgX is necessary for the development and optimization of various technological applications, including photovoltaic devices, solid-state electrolytes, and thermal management systems.

Yang *et al.* [4] reported ultralow κ_L of 0.20 and 0.18 $\mathrm{Wm^{-1}K^{-1}}$ for AgCl and AgBr at 300 K based on the conventional phonon gas model and first-principles calculations. Xia *et al.* [5] also calculated the κ_L of AgCl (0.6 $\mathrm{Wm^{-1}K^{-1}}$ at 300 K) by further including four-phonon scatterings and coherence contribution in the unified theory (UT) of thermal transport [6]. However, these theoretical studies still underestimate the experimental values of 1.10 (AgCl) and 1.05 $\mathrm{Wm^{-1}K^{-1}}$ (AgBr) [7]. In addition, Goetz *et al.* [8] reported an ultralow experimental κ_L of 0.42 $\mathrm{Wm^{-1}K^{-1}}$ at 300 K for AgI. Although Yan *et al.* [9] revealed that the fourth-order lattice anharmonicity is significant for the calculation of κ_L of AgI, the roles of higher-than-fourth-order phonon scatterings and the coherence thermal transport are not yet ascertained.

Atomic-level understanding of phonon-phonon scatterings plays a vital role in lattice thermal transport. Generally, three-phonon scattering is adequate to describe the lattice dynamics of the majority of crystals, while the four-phonon process has recently been demonstrated to play a significant role in strongly anharmonic materials with ultralow κ_L [10–12] and materials such as BAs [13] and TaN [14] that have severely restricted three-phonon phase space (P_3). Moreover, the considerable role of higher-than-fourth-order phonon scatterings was reported in Tl_3VSe_4 [15] and zinc-blende III–V compounds [16] such as InP, BN and InAs. Phonon frequency renormalization was also demonstrated in recent studies to be significant to predict the thermal property of strongly anharmonic materials, such as perovskites $SrTiO_3$ [17] and $Cs_2PbI_2Cl_2$ [18], and clathrate $Ba_8Ga_{16}Ge_{30}$ [19].

In this work, using accurate machine learning neuroevolution potentials (NEP) [20], we systematically investigate the lattice dynamics and thermal transport of AgX based on perturbation theory (PT) and the two-channel UT including both the population and coherence contributions [6, 21]. We show that the accurate extraction of the third-order interatomic force constants (IFCs) and the coherence contribution are of great importance to calculate the κ_L of AgX. For AgI, however, we find that the calculated κ_L significantly overestimates the experimental values [8] even after considering the renor-

---

* zzeng@ist.ac.at
† yuechen@hku.hk

malizations of the third- and fourth-order IFCs and the UT. The phonon linewidths calculated using the normal-mode-decomposition technique [22] based on molecular dynamics (MD) simulations [23] and NEP [20] indicate an important role of the higher-than-fourth-order phonon scatterings in AgI, which can be ascribed to the restrictions of the three- (P_3) and four-phonon phase spaces (P_4). Consequently, κ_L computed using MD phonon lifetimes within the UT shows a better agreement with the experimental results of AgI.

II. METHODS

Density functional theory (DFT) calculations of AgX are performed using the Vienna *ab initio* Simulation Package (VASP) [24] with the projector augmented wave (PAW) [25] method. The PBEsol [26] exchange-correlation functional is applied for all VASP calculations because the lattice parameters that it predicts well compare with the experiments, as shown in Table S1 of Supplementary Information (SI). We did not consider the effect of the thermal expansion since the lattice parameters of AgX undergo a minor change (<0.5%) over a temperature range of 300 K [27]. A plane wave energy cutoff of 500 eV and an energy convergence criterion of 10^{-8} eV are used in the self-consistent electronic calculations. Born effective charges and dielectric constants are included in our calculations. We construct the machine learning NEP [20] based on the accurate DFT calculations of structures generated from *ab-initio* MD simulations with a 250-atom supercell at temperatures up to 400 K under NVT ensemble. The renormalized second-order IFCs (IFCs2_TDEP) are extracted using the temperature-dependent effective potential (TDEP) scheme as implemented in the hiPhive package [28], following the work of Hellman *et al.* [29, 30]. GPUMD simulations [31] based on the NEP are performed at different temperatures, and 40 configurations at each temperature are extracted to fit the temperature-dependent cubic (IFCs3_MD) and quartic IFCs (IFCs4_MD). IFCs2_FDM and IFCs2_RDM are extracted using the finite displacement method (FDM) and rattle-displacement method (RDM), respectively. We also fit the third-order IFCs (IFCs3_RDM) via the RDM from a normal distribution with a standard deviation of 0.025 Å. It is noted that we subtract the harmonic contributions (0 K) from the total forces prior to fitting anharmonic IFCs [32]. The neighbouring cutoff distances for pairs, triplets, and quadruplets of AgX are 8.0, 7.0, and 6.0 Å, respectively. A q-mesh of 12×12×12 and a *scalebroad* of 0.5 are found to be adequate to obtain accurate phonon lifetimes of AgX. We use q meshes of 18×18×18 and 16×16×16 for the calculation of the weighted phase space (WPS) for AgCl and AgI, respectively. The WPS is defined as the sum of frequency-containing factors in the expression of three phonon transition probabilities and is expressed [33]:

$$W_\lambda^{\pm} = \frac{1}{2N} \sum_{\lambda',\lambda''} \left[\begin{array}{c} 2\left(f^0_{\lambda'} - f^0_{\lambda''}\right) \\ f^0_{\lambda'} + f^0_{\lambda''} + 1 \end{array} \right] \frac{\delta\left(\omega_\lambda \pm \omega_{\lambda'} - \omega_{\lambda''}\right)}{\omega_\lambda \omega_{\lambda'} \omega_{\lambda''}} \tag{1}$$

where N is the number of uniformly spaced q points in the Brillouin zone, $W_\lambda^{\pm}$ represents the absorption (+) and emission (-) processes.

Phonon power spectra are obtained by projecting the atomic velocities from MD simulations with NEP onto the temperature-dependent phonon eigenvectors using the normal-mode-decomposition technique [22]. Lattice thermal conductivity ($\kappa_\mathrm{L}^\mathrm{p+c}$) is contributed by diagonal (population $\kappa_\mathrm{L}^\mathrm{p}$) and off-diagonal (coherence $\kappa_\mathrm{L}^\mathrm{c}$) terms following the UT proposed by Simoncelli *et al.* [6]. The $\kappa_\mathrm{L}^\mathrm{c}$, which originates from the wave-like tunnelling of phonons, can be expressed as:

$$\begin{aligned} \kappa_\mathrm{L}^\mathrm{c} = {} & \frac{\hbar^2}{k_\mathrm{B} T^2 N V} \sum_{\boldsymbol{q}} \sum_{j,j'}^{j \neq j'} \frac{\omega(\boldsymbol{q})_j + \omega(\boldsymbol{q})_{j'}}{2} U(\boldsymbol{q})_{j,j'} U(\boldsymbol{q})_{j',j} \\ & \times \frac{\omega(\boldsymbol{q})_j n(\boldsymbol{q})_j \left(n(\boldsymbol{q})_j + 1\right) + \omega(\boldsymbol{q})_{j'} n(\boldsymbol{q})_{j'} \left(n(\boldsymbol{q})_{j'} + 1\right)}{4\left(\omega(\boldsymbol{q})_j - \omega(\boldsymbol{q})_{j'}\right)^2 + \left(\gamma(\boldsymbol{q})_j + \gamma(\boldsymbol{q})_{j'}\right)^2} \\ & \times \left(\gamma(\boldsymbol{q})_j + \gamma(\boldsymbol{q})_{j'}\right), \end{aligned} \tag{2}$$

where V is the volume of the unit cell, T is the temperature, N is the total number of sampled wave vectors and k_B is the Boltzmann constant. $n(\boldsymbol{q})_j$, $\omega(\boldsymbol{q})_j$ and $\gamma(\boldsymbol{q})_j$ are the equilibrium Bose–Einstein distribution, phonon frequency and phonon linewidth for branch j at wave vector $\boldsymbol{q}$, respectively. $U(\boldsymbol{q})_{j,j'}$ is the off-diagonal terms of the velocity matrix when $j \neq j^{'}$. We note that $\kappa_\mathrm{L}^\mathrm{p}$ can be calculated from equation (1) based on the phonon gas model when $j = j^{'}$. Additionally, the temperature-dependent κ_L of AgI is also calculated from the homogeneous non-equilibrium molecular dynamics (HNEMD) simulations [34, 35].

III. RESULTS AND DISCUSSION

To understand the discrepancy between experiments [36–38] and the existing first-principles calculation [4] for the κ_L of AgCl, we first compute the $\kappa_\mathrm{L}^\mathrm{p}$ using the IFCs2_FDM and IFCs3_RDM with PBE functional. It is seen from Figure 1(a) that our result is close to that of Yang *et al.* [4]. Note that the third-order IFCs of Yang *et al.* were extracted using the Phono3py package [43] with an atomic displacement of 0.03 Å. Similar to the results of Yang *et al.* [4], our $\kappa_\mathrm{L}^\mathrm{p}$ also significantly underestimates the experiments [36–38]. Despite the coherence term being included, the $\kappa_\mathrm{L}^\mathrm{p+c}$ is still lower than the experimental values. After using PBEsol functional rather than PBE functional, the $\kappa_\mathrm{L}^\mathrm{p}$ largely increases from 0.187 to 0.425 $\mathrm{Wm^{-1}K^{-1}}$ at 300 K, as displayed in Figure S4(a,b). Despite a considerable improvement being achieved for the calculated $\kappa_\mathrm{L}^\mathrm{p}$ of AgCl when PBEsol functional is used

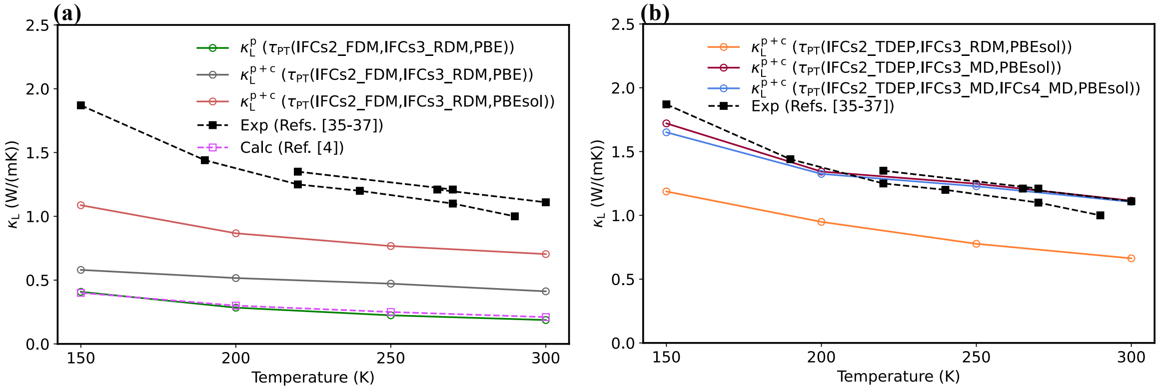

FIG. 1. (a, b) temperature-dependent κ_L of AgCl calculated using different sets of IFCs with PBE and PBEsol functional under the UT [6]. IFCs2, IFCs3, and IFCs4 stand for the second-, third-, and fourth-order IFCs, respectively. Configurations used for fitting the IFCs are generated by performing MD simulations [31] based on our NEP, and via the RDM from a normal distribution with a standard deviation of 0.025 Å. IFCs2_FDM and IFCs2_TDEP are extracted using the FDM and TDEP methods, respectively. The black solid symbols represent the experimental results taken from Refs. [36–38]. The purple square symbols stand for the theoretical data reported in Ref. [4].

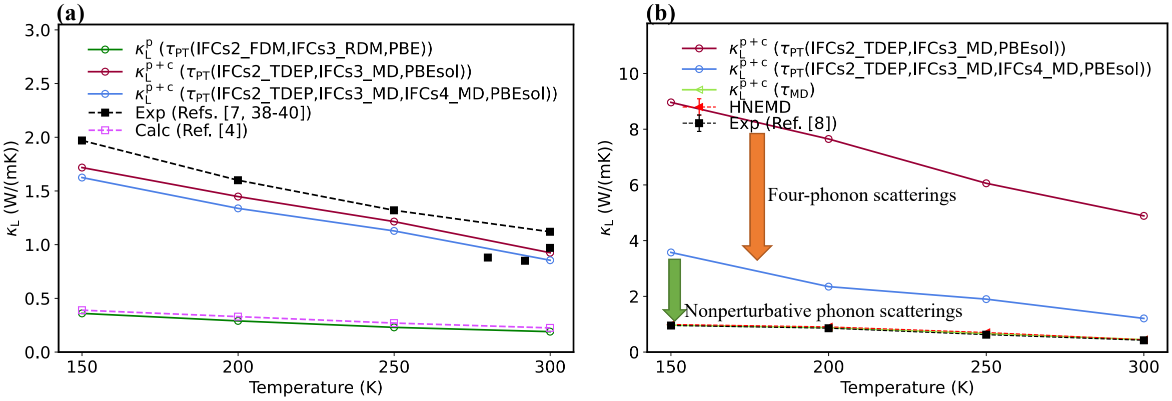

FIG. 2. (a) temperature-dependent κ_L^{p+c} of AgBr calculated using different sets of IFCs under the UT [6]. The black solid symbols represent the experimental results from Refs. [7, 39–41]. The mallow purple hollow symbols stand for the theoretical data reported in Ref. [4]. (b) κ_L^{p+c} of AgI computed using the different sets of IFCs. κ_L calculated using the phonon lifetimes (τ_{MD}) extracted from MD simulations and that from HNEMD simulations [34, 42] based on NEP are also shown for comparisons. The black solid symbols represent the experimental results from Ref. [8].

instead of PBE functional, the κ_L^{p+c} still significantly underestimates the experimental values.

We then study the phonon frequency renormalization of AgCl using the TDEP method [29, 30] based on NEP from 150 to 300 K, as displayed in Figure S3(a), where experimental values [44] of AgCl at 78 K are also included, showing a good agreement with our calculations. The phonon frequencies of AgCl generally show a weak temperature dependence, suggesting that the phonon frequency renormalization plays a minor role in predicting the κ_L of AgCl. This is different from AgI, as shown in Figure S3(b), or other strongly anharmonic materials such as perovskites $SrTiO_3$ [17] and $Cs_2PbI_2Cl_2$ [18], and clathrate $Ba_8Ga_{16}Ge_{30}$ [19], where the frequencies of low-frequency phonons show significant temperature dependence. Therefore, when we replace IFCs2_FDM with the temperature-renormalized IFCs2_TDEP, κ_L^{p+c} only changes slightly, confirming that phonon frequency renormalization is insignificant to computing the κ_L of AgCl, as displayed in Figure 1(a,b).

A recent study has demonstrated that largely displaced configurations are necessary to accurately extract the third-order IFCs for group-III phosphides [45]. Thus, we further investigate a different method for calculating the third-order IFCs and the effect on the κ_L of AgCl. The calculated κ_L^p increases significantly when we use IFCs3_MD, as shown in Figure S4(c,d), illustrating that an accurate calculation of the third-order IFCs is of great significance to predicting the κ_L of AgCl. Once the coherence contribution is also considered, a good agreement is obtained with the experimental results [36–38], as shown in Figure 1(b). The third-order IFCs calculated based on

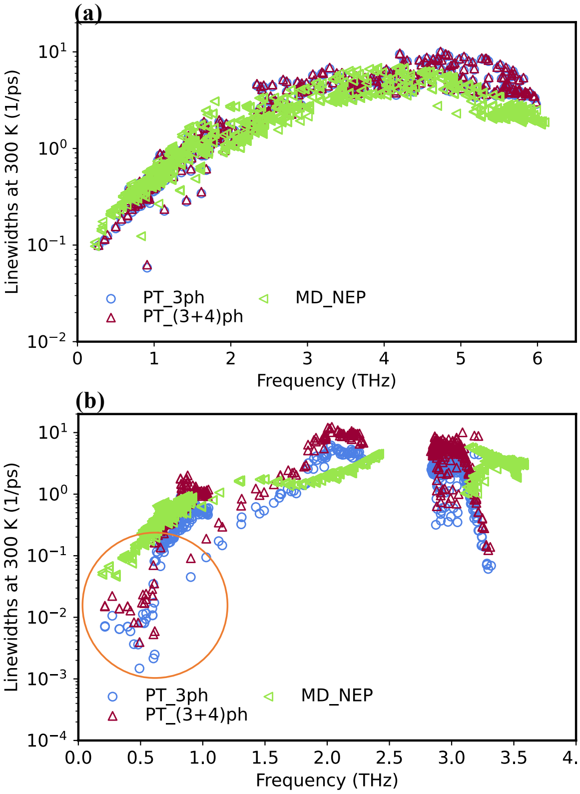

FIG. 3. Phonon linewidths of AgCl (a) and AgI (b) calculated from PT and MD simulations at 300 K. PT_3ph and PT_(3+4)ph represent the phonon linewidths computed using only the third-order and both of the third- and fourth-order IFCs, respectively. MD_NEP denotes the phonon linewidths calculated from MD simulations using our NEP.

MD configurations can decrease the phonon linewidths, as shown in Figure S5(b), and thus increase the $\kappa_{\mathrm{L}}^{\mathrm{p}}$. The atomic displacements of Ag and Cl atoms increase significantly with elevating temperature, as described by the comparably large mean square displacements in Figure S9. Therefore, extracting the third-order IFCs of AgCl from configurations generated by MD simulations is more reasonable.

We further extend our calculations to silver halides AgBr and AgI, and the results are shown in Figure 2. We find that the $\kappa_{\mathrm{L}}^{\mathrm{p+c}}$ of AgBr computed using IFCs2_TDEP and IFCs3_MD with PBEsol functional agrees well with the experimental results [39–41], while for AgI, the calculated $\kappa_{\mathrm{L}}^{\mathrm{p+c}}$ apparently overestimates the experiments [8]. When the four-phonon scatterings are also considered, the $\kappa_{\mathrm{L}}^{\mathrm{p+c}}$ significantly decreases from 4.88 to 1.21 $\mathrm{Wm^{-1}K^{-1}}$ at 300 K, but it still overestimates the experimental value (0.42 $\mathrm{Wm^{-1}K^{-1}}$), as shown in Figure 2(b). We further compute the phonon linewidths from PT using the IFCs fitted to MD configurations at 300 K, as shown in Figure 3(b). It is seen that the four-phonon linewidths are non-negligible, especially for the low-frequency modes, which usually contribute most to the thermal transport. In addition, we have calculated the temperature-dependent κ_{L} of AgI from HNEMD simulations with our NEP, and a good agreement with the experiment [8] is observed, as shown in Figure 2(b).

The overestimated $\kappa_{\mathrm{L}}^{\mathrm{p+c}}$ of AgI obtained from UT may be related to the inaccurate phonon linewidths; thus, we compare the phonon linewidths obtained from PT with that obtained from MD simulations using the normal-mode-decomposition technique [22], as displayed in Figure 3(b). We find that the MD phonon linewidths, which include full-order lattice anharmonicity, are significantly larger than those obtained from PT, suggesting that the higher-than-fourth-order lattice anharmonicity can be crucial for calculating the phonon linewidths and thus the κ_{L} of AgI. Therefore, we further compute the $\kappa_{\mathrm{L}}^{\mathrm{p+c}}$ using the MD phonon lifetimes τ_{MD}, and it shows a better agreement with the experimental values [8] and the HNEMD simulations over a temperature range from 150 to 300 K, as shown in Figure 2(b). We also find that the population term (0.21 $\mathrm{Wm^{-1}K^{-1}}$) of AgI is comparable with the coherence's contribution (0.23 $\mathrm{Wm^{-1}K^{-1}}$) at 300 K, as displayed in Figure S8, indicating that the coherence channel is of great importance to describing the thermal transport. On the other hand, we find that the difference of the phonon linewidths of AgCl between PT_3ph, PT_(3+4)ph, and MD_NEP is much smaller, as shown in Figure 3(a), suggesting that the higher-than-third-order lattice anharmonicity is insignificant to the lattice thermal transport.

To further reveal the different thermal transport mechanisms between AgCl and AgI, we calculate the three- and four-phonon WPS, as shown in Figure 4(a,b). From the phonon dispersions of AgI given in Figure S3(b), we can observe that the transverse acoustic (TA) branches ($\sim$ 0.7 THz) are almost non-dispersive near the high symmetry X-point, and the energy of the longitudinal acoustic (LA) branch is higher than double of the energy of the TA branches. Moreover, as pictorially drawn in Figure S11 (b), the combination of one TA phonons (TA1 or TA2) and one LA phonons can easily create one new LA phonons and one TA phonons (TA1 or TA2) through the four-phonon recombination process due to the automatic satisfaction of energy and momentum conservation. In comparison, the absorption of three-phonon scattering is limited by the energy conservation, as depicted in Figure S11 (a). Therefore, due to the conservations of phonon energy and momentum, three-phonon channels involving the low-frequency phonons are restricted, as indicated by the highlighted dip in Figure 4(a) for AgI. In contrast, no restriction on the three-phonon phase space is observed for AgCl. In addition, for the four-phonon WPS shown in Figure 4(b), we see that the redistribution channel is also restricted for the low-frequency phonons (below 0.5 THz) in AgI. Thus, the simultaneous restrictions of the three- and four-phonon WPS at low-frequency regions can lead to a more important role of the higher-order lattice anharmonicity in the thermal transport of AgI.

Although the significant role of the higher-than-fourth-

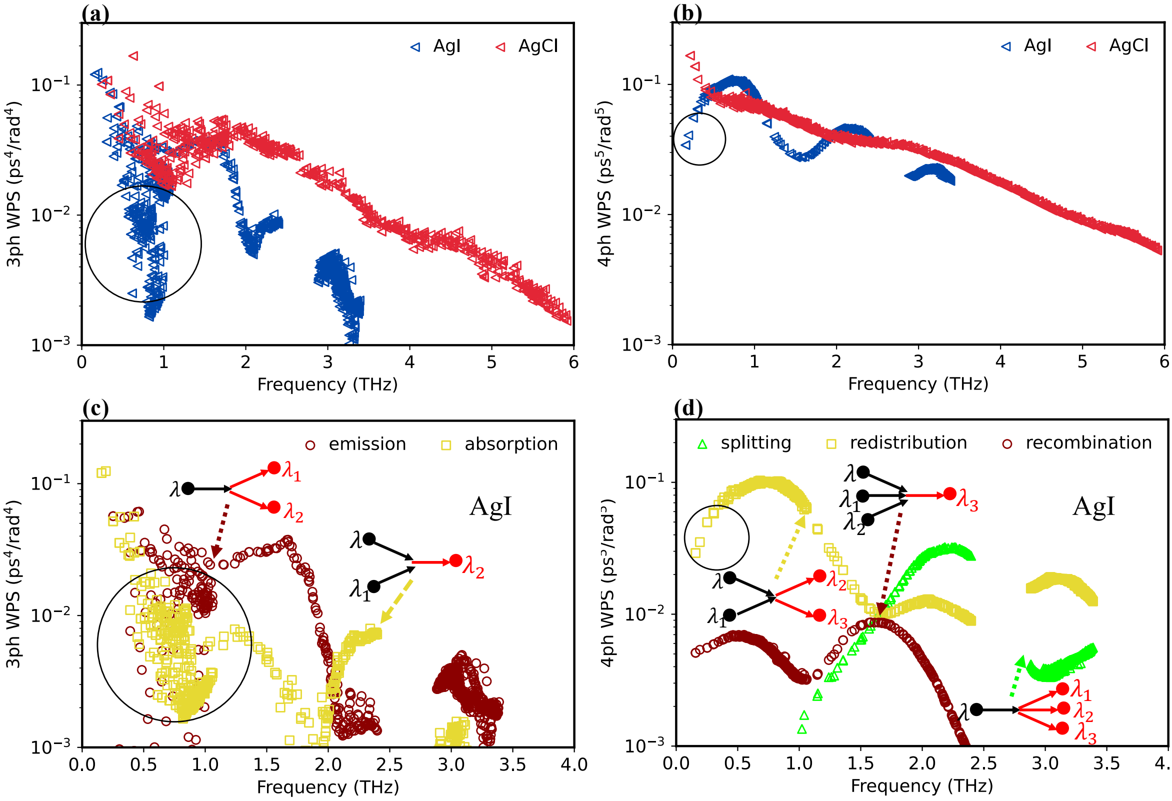

FIG. 4. Three- (a) and four-phonon (b) WPS of AgCl and AgI at 300 K. Mode-resolved three- (c) and four-phonon (d) WPS of AgI calculated at 300 K. Restricted phase space is observed inside the circled areas.

order lattice anharmonicity in the specific optical phonon modes at the zone-center has been demonstrated in zinc-blende III–V compounds [16] such as InP and BN, a study over the entire Brillouin zone is challenging due to the complex PT framework. Herein, we take AgI as an example and further calculate the phonon linewidths using the normal-mode-decomposition technique [22] and MD simulations based on a Taylor expansion force constant potential (FCP) [46] at 100 K, as shown in Figure S6(b). Results are obtained only at low temperatures because the MD simulations based on the FCP of AgI become unstable over 100 K. We observe that the phonon linewidths computed using NEP and the sixth-order FCP at 100 K are comparable, especially those of the low-frequency phonons, indicating that the seventh- or higher-order lattice anharmonicity plays a minor role in the phonon scattering of AgI at low temperatures. However, the phonon linewidths calculated based on the fourth-order FCP are much smaller than those from the sixth-order FCP at the low-frequency (∼ 0.2-0.8 THz) region, suggesting the importance of the fifth- and sixth-order lattice anharmonicity in the accurate calculation of the phonon linewidths and the κ_L of AgI. In other words, it is necessary to consider the higher-than-fourth-order lattice anharmonicity when calculating the κ_L of AgI even at low temperatures.

IV. CONCLUSION

In summary, using accurate machine learning NEP, we systematically study the phonon thermal transport of AgX under the framework of UT and MD simulations. Our results show that an accurate calculation of the third-order IFCs is important to predict the κ_L of AgX, and we also demonstrate that coherence contribution is considerable in these materials. Our MD simulations with NEP explicitly demonstrate the important contribution of the higher-than-fourth-order phonon scattering to the phonon linewidths and the κ_L of AgI. Our theoretical analysis suggests that this can be attributed to the simultaneous restrictions of P_3 and P_4. Thus, the κ_L calculated using the MD phonon linewidths agree better with the experiments and the HNEMD simulations of AgI.

ACKNOWLEDGMENTS

This work is supported by the Research Grants Council of Hong Kong (17318122 and 17306721). The authors are grateful for the research computing facilities offered by ITS, HKU. ZZ acknowledges the European Union's horizon 2020 research and innovation program under the Marie Skłodowska-Curie grant agreement No.

101034413.

---

[1] N. Kakuta, N. Goto, H. Ohkita, and T. Mizushima, Silver bromide as a photocatalyst for hydrogen generation from ch3oh/h2o solution, The Journal of Physical Chemistry B **103**, 5917 (1999).

[2] X. Yang, Z. Xiong, Y. Chen, Y. Ren, L. Zhou, H. Li, Y. Zhou, F. Pan, and S.-T. Han, A self-powered artificial retina perception system for image preprocessing based on photovoltaic devices and memristive arrays, Nano Energy **78**, 105246 (2020).

[3] T. Takahashi, E. Nomura, and O. Yamamoto, Solid state ionics. high ionic conductivity solid in silver halide-silver sulphate system, Journal of Applied Electrochemistry **2**, 51 (1972).

[4] X. Yang, Z. Dai, Y. Zhao, and S. Meng, Superhigh thermoelectric figure of merit in silver halides AgCl and AgBr from first principles, arXiv:1904.06010 (2019).

[5] Y. Xia, V. I. Hegde, K. Pal, X. Hua, D. Gaines, S. Patel, J. He, M. Aykol, and C. Wolverton, High-throughput study of lattice thermal conductivity in binary rocksalt and zinc blende compounds including higher-order anharmonicity, Physical Review X **10**, 041029 (2020).

[6] M. Simoncelli, N. Marzari, and F. Mauri, Unified theory of thermal transport in crystals and glasses, Nature Physics **15**, 809 (2019).

[7] R. Ross, P. Andersson, and G. Bäckström, Thermal conductivity and heat capacity of solid AgCl under pressure, International Journal of Thermophysics **2**, 289 (1981).

[8] M. Goetz and J. Cowen, The thermal conductivity of silver iodide, Solid State Communications **41**, 293 (1982).

[9] Y. Wang, Q. Gan, M. Hu, J. Li, L. Xie, and J. He, Anharmonic lattice dynamics and the origin of intrinsic ultralow thermal conductivity in AgI materials, Physical Review B **107**, 064308 (2023).

[10] Z. Zeng, C. Zhang, H. Yu, W. Li, Y. Pei, and Y. Chen, Ultralow and glass-like lattice thermal conductivity in crystalline $BaAg_2Te_2$: Strong fourth-order anharmonicity and crucial diffusive thermal transport, Materials Today Physics **21**, 100487 (2021).

[11] Y. Xia, K. Pal, J. He, V. Ozoliņš, and C. Wolverton, Particlelike phonon propagation dominates ultralow lattice thermal conductivity in crystalline Tl_3VSe_4, Physical Review Letters **124**, 065901 (2020).

[12] N. Ouyang, C. Wang, and Y. Chen, Role of alloying in the phonon and thermal transport of SnS-SnSe across the phase transition, Materials Today Physics , 100890 (2022).

[13] T. Feng, L. Lindsay, and X. Ruan, Four-phonon scattering significantly reduces intrinsic thermal conductivity of solids, Physical Review B **96**, 161201 (2017).

[14] A. Kundu, X. Yang, J. Ma, T. Feng, J. Carrete, X. Ruan, G. K. Madsen, and W. Li, Ultrahigh thermal conductivity of θ-phase tantalum nitride, Physical Review Letters **126**, 115901 (2021).

[15] Z. Zeng, C. Zhang, Y. Xia, Z. Fan, C. Wolverton, and Y. Chen, Nonperturbative phonon scatterings and the two-channel thermal transport in Tl_3VSe_4, Physical Review B **103**, 224307 (2021).

[16] X. Yang, T. Feng, J. Li, and X. Ruan, Evidence of fifth-and higher-order phonon scattering entropy of zone-center optical phonons, Physical Review B **105**, 115205 (2022).

[17] Q. Wang, Z. Zeng, and Y. Chen, Revisiting phonon transport in perovskite $SrTiO_3$: Anharmonic phonon renormalization and four-phonon scattering, Physical Review B **104**, 235205 (2021).

[18] Z. Zeng, C. Chen, C. Zhang, Q. Zhang, and Y. Chen, Critical phonon frequency renormalization and dual phonon coexistence in layered ruddlesden-popper inorganic perovskites, Physical Review B **105**, 184303 (2022).

[19] T. Tadano and S. Tsuneyuki, Quartic anharmonicity of rattlers and its effect on lattice thermal conductivity of clathrates from first principles, Physical Review Letters **120**, 105901 (2018).

[20] Z. Fan, Z. Zeng, C. Zhang, Y. Wang, K. Song, H. Dong, Y. Chen, and T. Ala-Nissila, Neuroevolution machine learning potentials: Combining high accuracy and low cost in atomistic simulations and application to heat transport, Physical Review B **104**, 104309 (2021).

[21] L. Isaeva, G. Barbalinardo, D. Donadio, and S. Baroni, Modeling heat transport in crystals and glasses from a unified lattice-dynamical approach, Nature Communications **10**, 1 (2019).

[22] A. Carreras, A. Togo, and I. Tanaka, DynaPhoPy: A code for extracting phonon quasiparticles from molecular dynamics simulations, Computer Physics Communications **221**, 221 (2017).

[23] T. Hansson, C. Oostenbrink, and W. van Gunsteren, Molecular dynamics simulations, Current Opinion in Structural Biology **12**, 190 (2002).

[24] G. Kresse and J. Furthmüller, Efficient iterative schemes for *ab initio* total-energy calculations using a plane-wave basis set, Physical Review B **54**, 11169 (1996).

[25] P. E. Blöchl, Projector augmented-wave method, Physical Review B **50**, 17953 (1994).

[26] J. P. Perdew, A. Ruzsinszky, G. I. Csonka, O. A. Vydrov, G. E. Scuseria, L. A. Constantin, X. Zhou, and K. Burke, Restoring the density-gradient expansion for exchange in solids and surfaces, Physical Review Letters **100**, 136406 (2008).

[27] B. Lawn, Thermal expansion of silver halides, Acta Crystallographica **16**, 1163 (1963).

[28] F. Eriksson, E. Fransson, and P. Erhart, The hiPhive package for the extraction of high-order force constants by machine learning, Advanced Theory and Simulations **2**, 1800184 (2019).

[29] O. Hellman, P. Steneteg, I. A. Abrikosov, and S. I. Simak, Temperature dependent effective potential method for accurate free energy calculations of solids, Physical Review B **87**, 104111 (2013).

[30] O. Hellman, I. Abrikosov, and S. Simak, Lattice dynamics of anharmonic solids from first principles, Physical Review B **84**, 180301 (2011).

[31] Z. Fan, Y. Wang, P. Ying, K. Song, J. Wang, Y. Wang, Z. Zeng, K. Xu, E. Lindgren, J. M. Rahm, *et al.*, GPUMD: A package for constructing accurate machine-

learned potentials and performing highly efficient atomistic simulations, arXiv:2205.10046 (2022).

[32] Y. Xia, V. Ozoliņš, and C. Wolverton, Microscopic mechanisms of glasslike lattice thermal transport in cubic $Cu_{12}Sb_4S_{13}$ tetrahedrites, Physical Review Letters **125**, 085901 (2020).

[33] W. Li and N. Mingo, Ultralow lattice thermal conductivity of the fully filled skutterudite $ybfe_4sb_{12}$ due to the flat avoided-crossing filler modes, Physical Review B **91**, 144304 (2015).

[34] Z. Fan, H. Dong, A. Harju, and T. Ala-Nissila, Homogeneous nonequilibrium molecular dynamics method for heat transport and spectral decomposition with many-body potentials, Physical Review B **99**, 064308 (2019).

[35] D. J. Evans, Homogeneous NEMD algorithm for thermal conductivity—application of non-canonical linear response theory, Physics Letters A **91**, 457 (1982).

[36] A. Maqsood, M. Anis-ur Rehman, K. Kamran, and I. H. Gul, Thermophysical properties of AgCl in the temperature range 77–300 K, Journal of Physics D: Applied Physics **37**, 1845 (2004).

[37] D. R. Lide, *CRC Handbook of Chemistry and Physics*, Vol. 85 (CRC press, 2004).

[38] K. A. McCarthy and S. S. Ballard, New data on the thermal conductivity of optical crystals, JOSA **41**, 1062 (1951).

[39] K. Kamran, M. Anis-ur Rehman, and A. Maqsood, Thermal and electrical properties of crystalline silver bromide, Journal of Physics D: Applied Physics **40**, 869 (2007).

[40] T. Pochapsky, Heat capacity and thermal diffusivity of silver bromide, The Journal of Chemical Physics **21**, 1539 (1953).

[41] E. Washburn, International critical tables, 1st edn, vol. i (1926).

[42] B. Dongre, T. Wang, and G. K. Madsen, Comparison of the green–kubo and homogeneous non-equilibrium molecular dynamics methods for calculating thermal conductivity, Modelling and Simulation in Materials Science and Engineering **25**, 054001 (2017).

[43] L. Chaput, A. Togo, I. Tanaka, and G. Hug, Phonon-phonon interactions in transition metals, Physical Review B **84**, 094302 (2011).

[44] K. Fischer, Lattice dynamics and anharmonic effects in AgCl, Physica Status Solidi (B) **66**, 295 (1974).

[45] B. Dongre, J. Carrete, N. Mingo, and G. K. Madsen, Thermal conductivity of group-iii phosphides: The special case of GaP, Physical Review B **106**, 205202 (2022).

[46] J. Brorsson, A. Hashemi, Z. Fan, E. Fransson, F. Eriksson, T. Ala-Nissila, A. V. Krasheninnikov, H.-P. Komsa, and P. Erhart, Efficient calculation of the lattice thermal conductivity by atomistic simulations with *ab initio* accuracy, Advanced Theory and Simulations **5**, 2100217 (2022).